Flow characterization of flickering methane/air diffusion flames using particle image velocimetry

G. Papadopoulos, R.A. Bryant, W.M. Pitts

472

Abstract Phase-resolved measurements of the velocity field in acoustically forced, flickering laminar co-flowing methane/air diffusion flames were made. Identical flames have been studied extensively in the past in order to characterize the effects of the vortical structures responsible for the flicker on the flame structure, but the initial velocity perturbation and the velocity fields have not been reported previously. Phase-locked measurements of the instantaneous two-dimensional velocity field at ten phases within a full excitation cycle were made using particle image velocimetry. The velocity measurements were complemented by phase-resolved shadowgraphs recorded in the vicinity of the flame base. Measurements are reported for the two forcing conditions that have most often been studied for this burner. When integrated with the results of previous studies, these measurements provide a clearer picture of the interactions between the buoyancy-induced vortical structures and the flame sheets, as well as providing the initial conditions required for realistic modeling of these flames.

1
Introduction

Vortex interactions with flames play a key role in many practical combustion applications and, as a result, have been the focus of considerable study (Renard et al. 2000). Such interactions form the basis for understanding naturally flickering buoyancy-dominated diffusion flames. These flames exhibit natural flicker as a result of a buoyancy-induced flow instability attributed to the interaction

G. Papadopoulos (✉)
Dantec Dynamics Inc., 777 Corporate Drive,
Mahwah, NJ 07430, USA
E-mail: george.papadopoulos@dantecdynamics.com
Tel.: +1-201-5120037
Fax: +1-201-5120120

R.A. Bryant, W.M. Pitts
National Institute of Standards & Technology,
Building and Fire Research Laboratory,
Gaithersburg, MD 20899, USA

of strong vortical motions within the combusting regions of the flame (Hamins et al. 1992; Cetegen and Ahmed 1993; Cetegen and Dong, 2000). Under normal gravity conditions, the flames have a well-defined oscillation frequency which is inversely proportional to the square root of the burner diameter, D, and to a good approximation can be written as $f \approx 1.5/D^{1/2}$ Hz, with D given in meters. Despite the widespread natural occurrence of flame flickering, however, much of our current understanding of diffusion flame behavior is based on the experimental characterization of steady laminar flames. Detailed characterization of flickering flames is considerably more limited. This limitation is significant because ranges of flame properties, such as local strain and scalar dissipation rates, and flame residence times, are significantly broader in laminar time-varying diffusion flames. A better understanding of flickering flame behavior also promises to improve the current understanding of turbulent combustion systems, since a much wider range of local conditions is available to characterize the flame–flow interactions that are more dominant in turbulent flames.

Naturally occurring flickering flames are difficult to investigate experimentally because, even though the flickering frequency is well defined, there exist cycle-to-cycle variations. These variations lead to spatial and temporal averaging with a resulting loss in resolution, since it is usually not possible to record local experimental measurements throughout the flame during a single cycle. Conditional sampling (e.g., see Lingens et al. 1996) provides some improvement, but significant averaging still occurs. It has been found that it is possible to generate very repeatable time-varying diffusion flames by acoustically forcing the fuel flow at frequencies close to the natural oscillation frequency of the flame (Strawa and Cantwell 1985). Such flames can be characterized by repeated phase-averaged measurements. While not necessarily identical to the corresponding naturally flickering flame (acoustically forced flame structures are found to change with the degree of forcing), the flames are sufficiently similar to suggest that the governing physical mechanisms are the same. The ability to control the degree of forcing also offers an opportunity to control local flame conditions.

A seminal paper by Lewis et al. (1988) demonstrated the effectiveness of the approach. The authors applied a variety of experimental techniques, including flame imaging, laser-induced fluorescence imaging of the hydroxyl (OH) free radical, and particle tracking velocimetry to demonstrate that flame flickering is associated with the formation

of strong vortical structures with centers located outside the flame sheet. More importantly, they were able to demonstrate that a flame extinction observed over small regions of their flame occurred at positions where the strain rate was sufficiently high to extinguish a steady laminar diffusion flame.

Over the past several years, numerous investigations concerning acoustically forced flickering flames have been reported on a modified burner originally developed at the National Institute of Standards and Technology (NIST) for steady laminar flame studies (Santoro et al. 1983). Phase-resolved measurements that have been reported include laser-induced fluorescence imaging of OH (Smyth et al. 1993; Shaddix et al. 1994), CO (Everest et al. 1996), and polycyclic aromatics (Smyth et al. 1997), flame luminosity (Smyth et al. 1997), soot scattering (Smyth et al. 1993; Shaddix et al. 1994) extinction (Shaddix et al. 1994), soot field characterization using laser-induced incandescence (LII) (Shaddix and Smyth 1996), temperature measurements along lines across the flame using time-resolved thin-filament pyrometry (Pitts 1996; Pitts et al. 1998), infrared tunable diode laser measurements of carbon monoxide (Skaggs and Miller 1996), and characterization of local soot morphology within the flames (Zhang and Megaridis 1998). Many of the NIST results are summarized in an extensive database available on the World Wide Web (Smyth 2000). The experimental findings have been compared with a detailed two-dimensional modeling study designed to predict the flame structure and soot fields for the time-varying flame (Kaplan et al. 1996).

Even though the experimental characterization of time-varying flames on the NIST burner is extensive, a major limitation for the data set is that up to now there have been no experimental measurements of the corresponding velocity fields or even of the initial flow conditions. Early attempts to quantify the initial flow conditions using bubble flow meters and hot-wire anemometry were unsuccessful (Smyth et al. 1993). Two initial flow conditions have received the most attention in these previous studies, characterized by the voltage amplitude of the sinusoidal excitation. This voltage was measured at the loudspeaker of the original NIST burner, 0.75 V and 1.5 V, and the general descriptors "moderate" and "strong", respectively, were used to distinguish the two flame cases.

The present paper addresses the need for velocity field characterization of these time-varying flames by reporting phase-resolved particle image velocimetry (PIV) measurements for the two cases. In addition to PIV measurements, phase-resolved shadowgraphy was used to qualitatively investigate the refractive index field at the base of the flame, which was expected to correlate with the local temperature field, thus making apparent regions of cold fuel injection and ambient air entrainment.

2
Experimental setup

A schematic of the experimental arrangement is shown in Fig. 1. A second burner, identical in material and design to the one used by Smyth and co-workers at NIST, was built for the purpose of carrying out the PIV measurements. The shadowgraphy measurements were performed on the original burner, part of an initial stage to the investigation that also included visible flame imaging on both burners so as to accurately match the two flame cases on the second burner to those of the first.

2.1
Burner description

An unconfined, axisymmetric, laminar diffusion flame was established at atmospheric pressure on a co-annular burner consisting of an 11.1-mm-diameter fuel tube surrounded by a 101-mm-diameter air annulus. The 100-mm-tall air chamber was filled with glass beads followed by several fine mesh screens and a 25.4-mm-thick ceramic
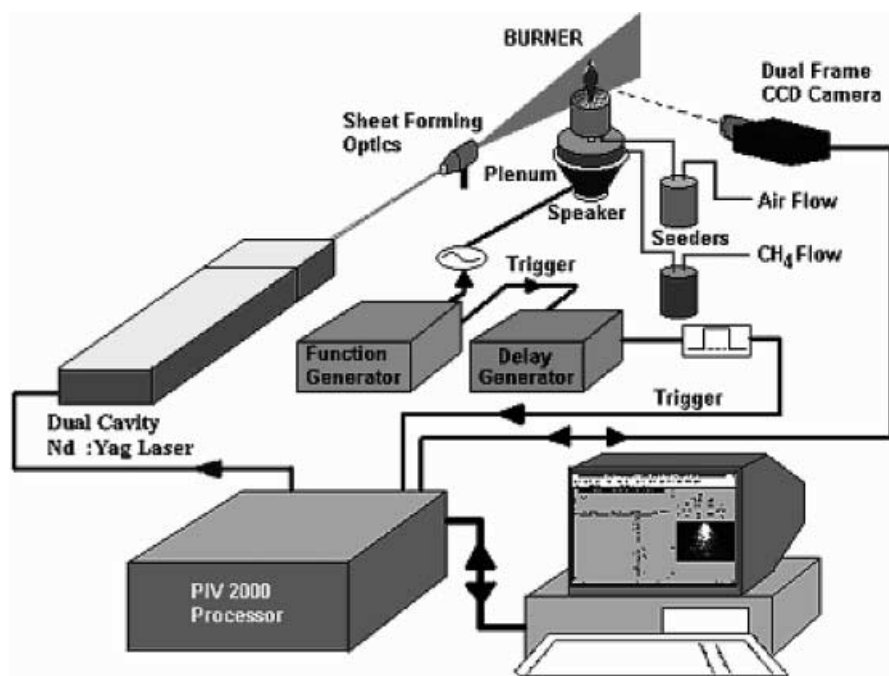

Fig. 1. Experimental setup of burner and PIV instrumentation for carrying out velocity measurements in the time-varying flames

honeycomb section with 1.5-mm-square cells. This arrangement was designed to provide an initially uniform flow velocity across the top of the annulus, as previously noted in earlier investigations using the same burner design. No beads or screens were used for flow conditioning in the 161-mm-long fuel tube. The tube was attached to a plenum below the air chamber, extending 6 mm into this chamber, and its exit was elevated 4 mm above the honeycomb. The plenum was 153 mm in diameter and 32 mm deep and was sealed on the bottom side with a 1-mm-thick rubber diaphragm.

A 20.3 cm (8-in.) standard speaker was mounted on the underside of the plenum to the bracket supporting the diaphragm. The speaker was sinusoidally excited using the voltage signal from a digital function generator. The excitation frequency was 10 Hz, and the output was set to the values (peak-to-peak measured at the speaker) appropriate for generating flames matching the previously investigated moderately and strongly forced flickering flames.

The fuel was "UCP"-grade methane (99% purity), introduced into the plenum at a constant rate of 0.452 L/min. The resulting bulk velocity (assuming room temperature flow) at the exit of the fuel tube was 77.7 mm/s. House-supply air flowed through the annulus at a rate of 38.0 L/min, yielding an average velocity of 79.0 mm/s
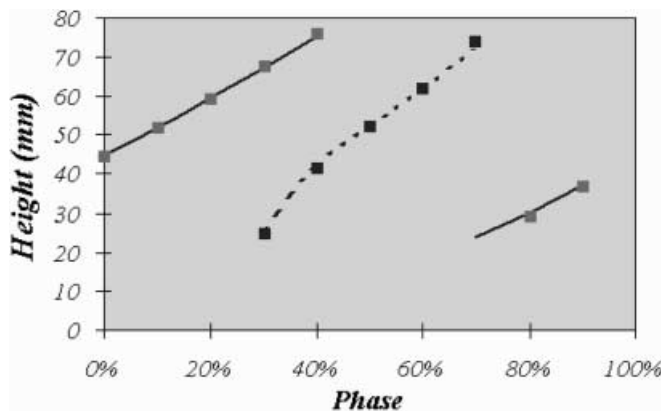

Fig. 2. Visible flame heights for the strongly perturbed case determined from recorded images at each of the ten phases (*symbols*) and compared to the visible flame heights reported by Smyth et al. (1993) (*lines*) (*dashed line with symbols* corresponds to clipped flame base–height measurement)

across the top. Both fuel and co-flow air were regulated using mass flow controllers separately calibrated for each fluid using a bubble flow meter. The calibration uncertainty of both controllers was less than 1%. (Reported uncertainties are at 95% confidence, unless otherwise noted.) Under these steady flow conditions the laminar diffusion flame had a visible height of 79 mm, in agreement with earlier measurements on the original burner reported by Smyth et al. (1993).

Even though the original and new burners were nominally identical, it was found that the flames generated by applying 0.75 V and 1.5 V sine waves to the speaker for the new burner differed significantly from the moderately and strongly forced flames previously investigated. A similar observation was reported by Skaggs and Miller (1996) and attributed to subtle differences in the way the rubber diaphragm was installed. By systematically varying the applied voltage of the sine wave for the new burner and comparing flame images for different phases, conditions were identified that provided nearly identical flames for the moderate and strong forcing conditions. As a demonstration of the success of this approach, Fig. 2 shows a comparison of the visible flame heights for the clipped flame, as well as the base of the upper flame (see Fig. 3) for the strong forcing case recorded using the two burners. The comparison is quite good. Results shown in Smyth et al. (1993) indicate that the flame shapes depend strongly on the voltage of the applied sine wave, providing additional evidence that the initial conditions for the cases on both burners are closely matched. Examples of flame luminosity results collected during the present investigation for the strongly perturbed flame are shown in Fig. 3. The images were obtained using the digital camera setup that was part of the PIV instrumentation described in detail in the following section. The field of view of the camera was 79.6 mm wide by 80.4 mm high. The images shown in Fig. 3 are a composite of two visualizations taken at two elevations, and cropped to arrive at a final image size of 47.6 mm wide by 160.7 mm high. The visualizations were performed at separate times, and the good match between image pairs for phases 50% to 70% demonstrate the repeatable behavior of the flame. A Schott BG-12 filter was placed in front of the lens to limit wavelength detection to the visible spectrum below approximately 530 nm. Mostly the strong radiation from soot particles is detected in this wavelength region, thus allowing
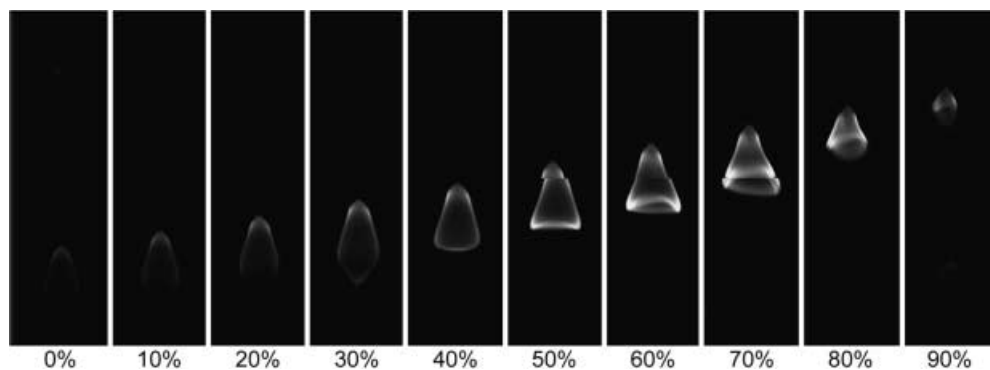

Fig. 3. Visible luminosity images for the strongly flickering flame case, obtained with a Schott BG-12 filter and 1-ms shutter window (images are gray scale reversed; each image size is 47.6 mm wide by 160.7 mm high)

comparison with similar images reported by Smyth et al. (1997).

2.2
PIV system and data analysis

A commercial PIV system from Dantec Dynamics Inc.[1] was used consisting of a laser illumination source, digital imaging device, and dedicated hardware and software for data analysis. The illumination source was a frequency-doubled, double-cavity Nd:YAG laser operating at a wavelength of 532 nm (200 mJ per pulse) and a pulse rate of 15 Hz. The overlapped core beams were expanded into a 20-degree diverging light sheet using focusable sheet-forming optics. At the measurement station, the sheet was approximately 1 mm thick and was aligned vertically along the diameter of the fuel tube (as shown in Fig. 1). Recording of particle image pairs was accomplished via a Kodak Megaplus ES1.0 8-bit double-frame CCD camera with a pixel format of 1,008×1,018. This type of camera eliminated image order ambiguity and allowed for the use of cross-correlation methods when determining velocity vectors. A band-pass filter centered at 532 nm (±15 nm) was placed in front of the camera lens to reduce flame luminosity effects on the acquired images. Processing of the images to derive vector maps was done via dedicated hardware for on-line correlation analysis by means of FFT-based algorithms implemented using programmable electronics. The correlator was housed inside a processor unit that contained a memory buffer and camera personality module that stored the camera response function (frame grabber equivalent for accessing camera logic and control), and a synchronization module for phase-locking the laser and camera activation sequences to an external trigger source. Once evaluated, a raw vector map data was passed to a personal computer for visualization and storage. Setting of data acquisition parameters and management of data was accomplished using dedicated software to interact with the programmable processor.

Seeding of the methane fuel and air co-flow was accomplished with 1.5-μm aluminum oxide particles introduced into the flow lines using separate cyclone seeders located downstream of the mass flow controllers. The seeders were equipped with bypasses to allow control of the seeding density. Seeding was initiated just prior to each data acquisition sequence to reduce particle accumulation in the burner annulus. During the course of the investigation, the burner was regularly flushed with clean air to discharge accumulated particles and minimize blockage effects on co-flow velocity uniformity. Furthermore, the introduction of seeding particles was not observed to affect the flame condition in the measurement area of interest. Flame characteristics, such as shape and temporal behavior, agreed quite well with earlier unseeded measurements performed by Smyth and co-workers.

A 40-mm-square viewing area was sampled along the centerplane of the flame during individual experiments. Separate velocity maps were recorded at two heights by traversing the burner relative to the imaging system in order to cover a total distance of 75 mm in the axial direction. A trigger-out signal from the function generator was input to a digital delay generator, which in turn was used to trigger the PIV processor at fixed phase delays within the excitation cycle. Four externally triggered ensembles of 18 recordings were acquired for each of the ten phases. The time separation between pulses was typically about 600 μs, yielding particle displacements of 15% to 20% of the square interrogation area length. A 64×64 pixel interrogation area at 50% overlap was selected, giving good dynamic range and signal-to-noise performance, with reasonable spatial resolution (approximately 2 mm). A peak-validation and moving average technique (as reported by Madsen and McCluskey 1994) were used to invalidate erroneous vectors prior to phase-averaging all 72 instantaneous realizations.

To investigate the initial conditions at the fuel tube exit, the camera was zoomed to a 26-mm square area surrounding the exit. Higher seeding concentrations close to the exit allowed for a 32×32 pixel interrogation area to be used for correlating particle displacement information between successive images. This resulted in a spatial resolution of approximately 0.7 mm. Relative particle displacements were maintained at 15–20% of the interrogation area size, yielding an estimated dynamic range of at best 200, given seeding density, homogeneity, and image contrast that tend to affect the accuracy of displacement vector estimation. Thus a velocity resolution of at most 1/200th of the maximum measured is assumed for all of the measurements reported herein. This corresponds to a minimum resolved velocity of approximately 10 mm/s and 2 mm/s for the field and inlet measurements, respectively. For each flame condition and at each phase, an ensemble of 36 instantaneous, phase-resolved measurements at the exit of the burner were averaged to construct mean profiles of the vertical and lateral velocities, W and U, respectively.

2.3
Shadowgraphy

Prior to initiating the PIV measurements, the PIV apparatus was re-arranged to qualitatively investigate the refractive index field of each flame case using simple shadowgraphy. These measurements were performed on the original burner used by Smyth and co-workers at NIST. Instead of using the sheet-forming optics to illuminate a diametric plane, the laser beam was first expanded and then focused onto a 2-mm glass sphere, which served as the point source for the shadowgraph (shown in Fig. 4). Scattered light from the sphere was then selectively collimated to a diameter of 50 mm and projected through the flame onto a screen located 190 cm from the center of the burner. Imaging of the shadowgraph was then performed using the CCD camera. Phase-locking to various times within the excitation cycle was performed in the same way as for the PIV measurements. To improve on the quality of the images, a reference shadow image at the

---

[1]Certain commercial equipment or materials are identified in this publication to specify adequately the experimental procedure. Such identification does not imply recommendation or endorsement by the National Institute of Standards and Technology, nor does it imply that the materials or equipment are necessarily the best available for this purpose.
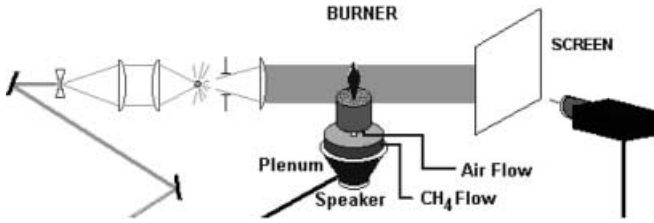
Fig. 4. Optical and recording setup for shadowgraphy measurements

flame off condition was first recorded and then subtracted from consecutive shadowgraphs.

3
Results

Plots of the centerplane velocity field obtained using the PIV technique are shown in Fig. 5 for both the moderately and strongly flickering flame cases. Each vector map is the statistical average of 72 phase-resolved realizations. The calculated vorticity component from the planar phase-averaged velocity data is shown in Fig. 6. Both the velocity field and vorticity contours are arranged to correspond to the phases for the OH radical and soot scattering images reported previously by Shaddix et al. (1994) and shown in Fig. 7 for comparison. The gray-scale coding of the contours in Fig. 5 and Fig. 6 denotes the magnitude of the velocity and vorticity fields, respectively.

The flow was buoyancy driven, as clearly indicated by the velocity magnitudes. Maximum velocities during certain phases of the cycle exceeded 1.8 m/s, more than 23 times the nominal bulk flow velocity of the fuel at the burner exit. Such high velocities were noticeable in areas above the instantaneous flame tip where a strong inward flow of surrounding gases was taking place. Comparable velocities were measured for both cases, with the moderately forced case exhibiting slightly greater velocity amplification.

Streamline traces in Fig. 5 make obvious the existence of strong vortical rings (as indicated by the radial symmetry) that initially form near the base of the flames and are then convected downstream with time. The vortical rings rotated from the co-flow side towards the flame and back out to the co-flow, thus in the process drawing cool co-flow air towards the flame centerline. In doing so, they forced the flame sheets towards the centerline. Flame clipping occurred when the entrained air reached the jet centerline. As expected, maximum streamline deflections towards the centerline occurred just before flame clipping, at phases 60% and 40% for the moderate and strong forcing cases, respectively. This is also made obvious in the vorticity maps of Fig. 6. Areas of strong vorticity form at the base of the flame, and move inward as the cycle progresses. Flame clipping occurs when these areas of opposing vorticity are the closest.

The locations of the vortical centers responsible for the streamlines were outside the regions imaged during the
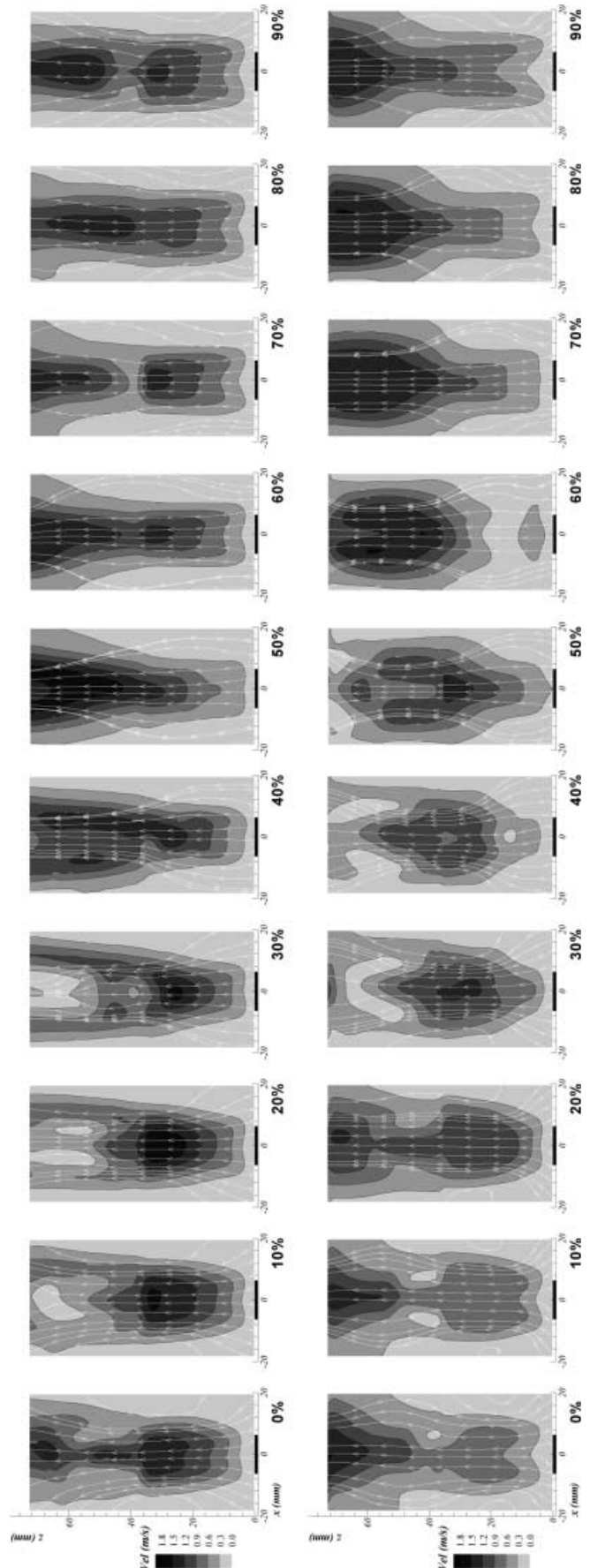
▶

Fig. 5. Velocity magnitude and streamline plots of phase-averaged PIV results along the centerplane for the moderately (*top*) and strongly (*bottom*) flickering flame cases: results from 10 phases in an excitation cycle, 0% at *left* and increasing to the *right*
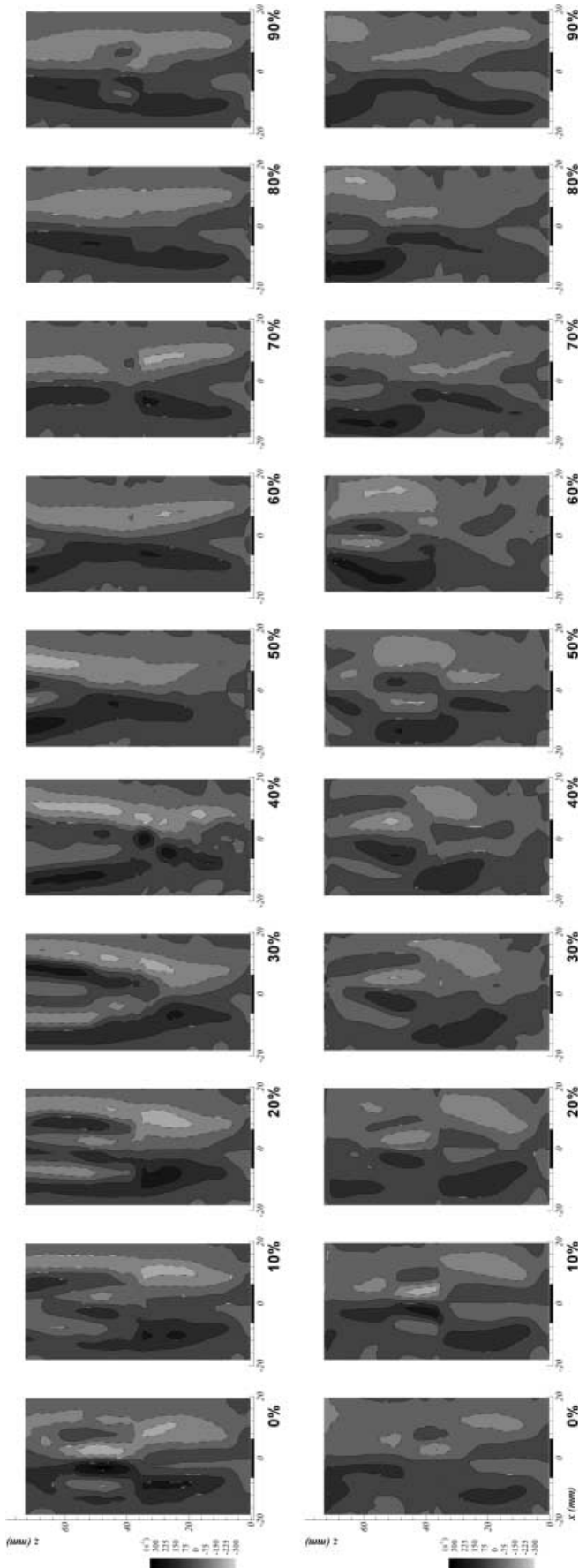
Fig. 6. Vorticity contours from phase-averaged PIV results along the centerplane for the moderately (*top*) and strongly (*bottom*) flickering flame cases: results from 10 phases in an excitation cycle, 0% at *left* and increasing to the *right*

PIV measurements. Unfortunately, it was not possible to make measurements further from the centerline owing to a fall-off in seeding levels associated with entrainment of air from beyond the region of the co-flow. Even so, it is clear from Figs. 5 and 6 that the vortical structures were centered in the surrounding co-flow at positions well removed from the flow zone (compare with the flame images in Fig. 7). It also appears likely that the distortions of the lower flame surfaces observed following flame splitting (see Fig. 7) resulted from interactions between the flame surface and these strong vortical structures.

Lewis et al. (1988) observed similar vortical structures during their investigation of acoustically forced laminar diffusion flames. These workers did not report full-phase resolved measurements, so it was not possible to track the formation and growth of the structures. However, detailed comparisons with flame structure measurements did indicate that, while the vortical structures were centered at locations well outside the flame sheet, their influence did extend into the flame zone and were responsible for the distinct appearance at the base of the upper section of the split flame. Interestingly, the vortical structures in the Lewis et al. flame were sufficiently strong to induce strain rates that were high enough to extinguish the flame over small regions of the upper flame base. This was not observed for the current flames (see Fig. 7).

In the modeling efforts of Kaplan et al. (1996), numerical tracking of fluid parcels in the flowfield passing through the maximum sooting region showed that flickering flames exhibit much longer residence times during which the local temperature and stoichiometries are favorable for soot production. Good quantitative agreement between computations and experiments was achieved at mid-flame heights, but discrepancies existed near the burner lip. These discrepancies were attributed to several factors, but a potentially important factor not discussed was the selection of initial conditions at the exit of the fuel tube. In the absence of detailed measurements in this region, parabolic pipe flow was assumed and a 10-Hz sinusoidal function of varying amplitude (a 75% velocity variation was found to provide the best agreement with experiments) was applied to the fuel inflow velocity.

In order to better characterize the initial flow conditions, detailed measurements of the velocity profile near (approx. 0.3 mm above) the fuel tube exit were performed during the present PIV investigation. The nearest profiles to the fuel tube exit resulting from these measurements are shown in Figs. 8 and 9 for the moderate and strong cases, respectively. Several interesting features can be identified by considering the vertical velocity components, W, for the two cases. As expected under no-slip flow conditions, axial velocities approached zero for the boundary-layer locations near the burner wall. Interestingly, axial flow velocities immediately outside the burner walls were increasing as the wall was approached. These velocities depended only weakly on phase angle. The flow acceleration was
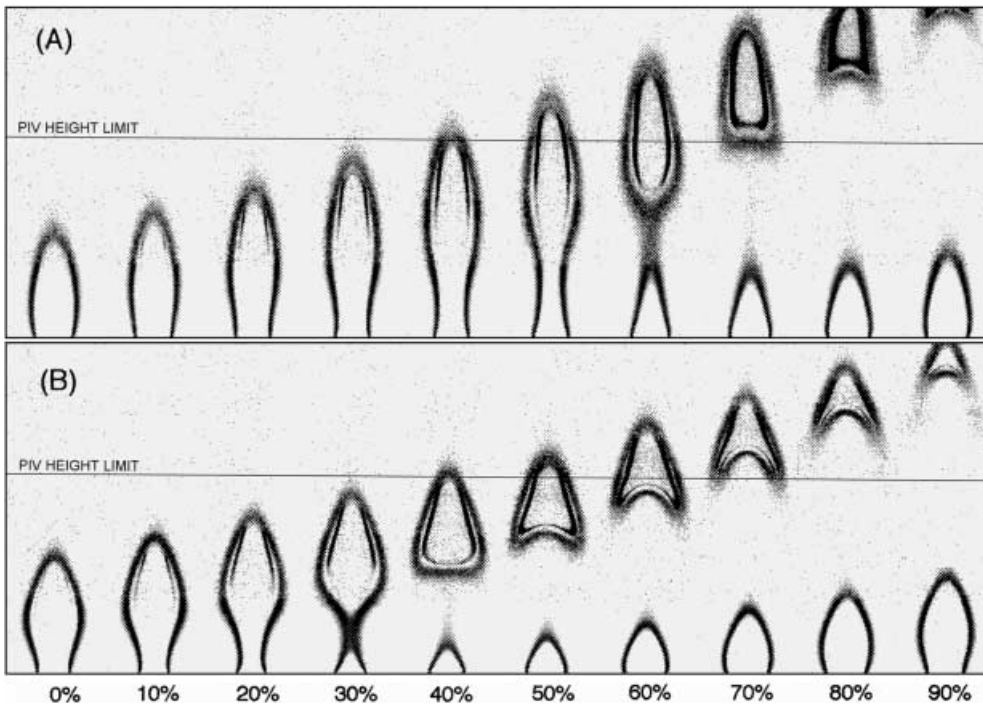
Fig. 7a, b. OH laser-induced fluorescence and soot-scattering images reported previously by Shaddix et al. (1994): **a** moderately flickering flame case; **b** strongly flickering flame case

probably due to entrainment associated with the presence of an attached flame on the burner. The fuel tube extended 4 mm above the honeycomb, so it favored such an attachment. Signs of an attached flame present at the lip of the fuel tube were also visible in the shadowgraph images to be discussed later.

For both cases, the velocity profiles above the fuel tube varied dramatically with phase. During times when the velocities were decreasing, the profiles had contours similar to those expected for parabolic flow. However, when the flow velocities began to increase, the profiles became strongly distorted with velocities near the center becoming lower than observed at more distant radial positions. For certain phases in both flames, simultaneous in-flow and out-flow occurred at different radial locations. Clearly, a parabolic flow profile is a poor approximation for the actual radial profiles present during these phases.

Note that the phases corresponding to lowest and highest observed velocities differed significantly for the moderately (60% and 0%, respectively) and strongly (30% and 80%, respectively) forced flames. During certain phases, especially for the strongly forced case, negative W velocities were measured, indicating that fluid was actually being sucked back into the fuel tube. The highest negative velocities (approximately twice the nominal bulk velocity) for the strongly forced flame were recorded for the 30% phase, which corresponded to the time in the cycle when the flame tip was about to clip (see Fig. 7). Much lower negative velocities were recorded for the moderately forcing case with the most negative velocity also corresponding to the phase when the flame tip was about to clip. Maximum observed velocities for the two cases were roughly three and four-and-a-half times higher than the nominal bulk velocity for moderate and strong forcing, respectively.
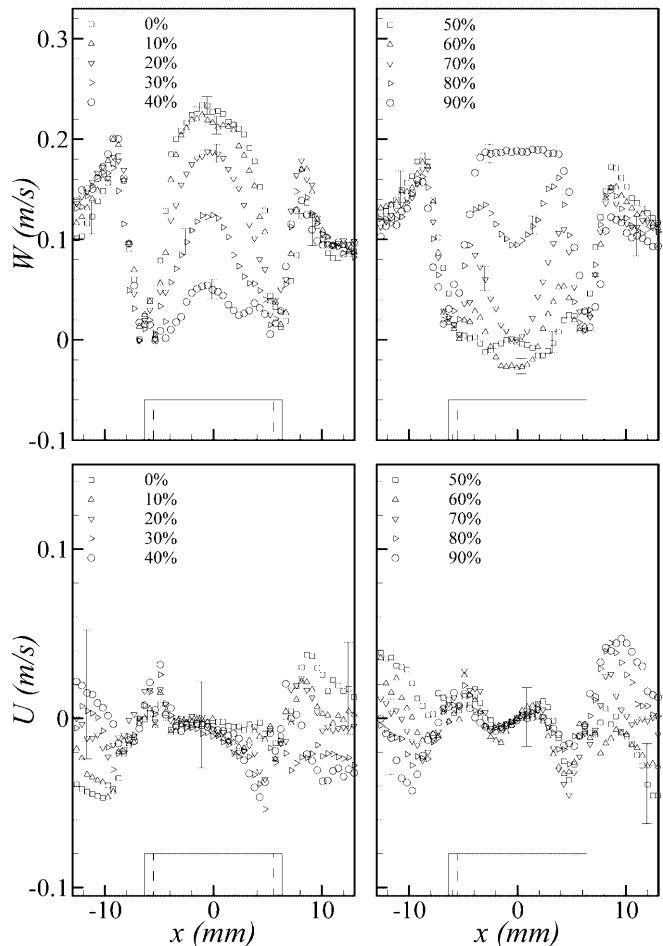

Fig. 8. Velocity profiles near the exit of the burner ($z=0.3$ mm) for the moderately flickering flame case
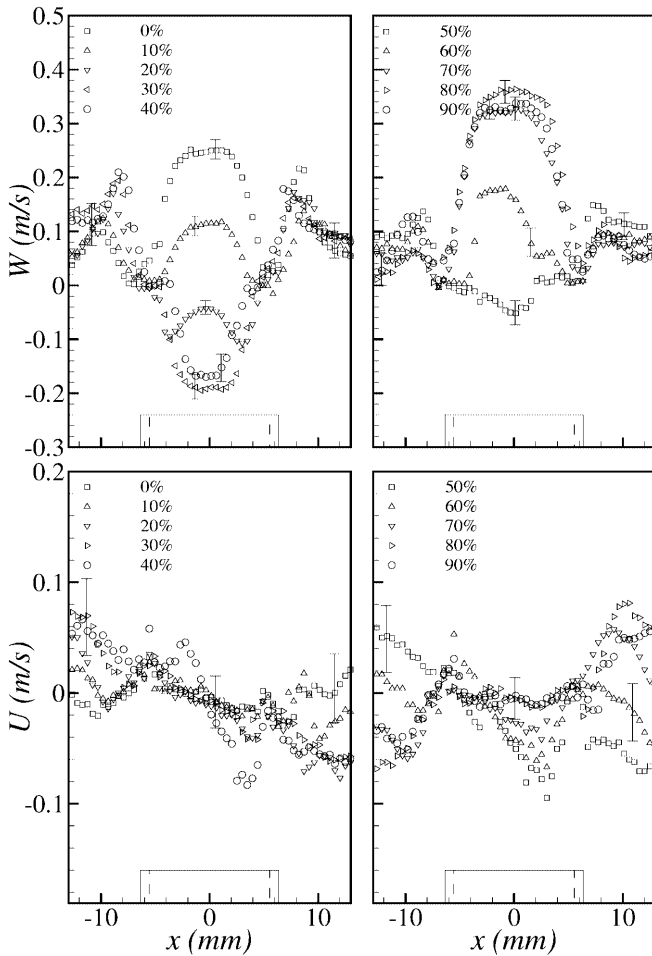
Fig. 9. Velocity profiles near the exit of the burner ($z=0.3$ mm) for the strongly flickering flame case

The radial components of the velocity profiles had different dependencies on radial position from those observed for the axial components. For positions outside the fuel tube, the radial velocities depended quite strongly on phase angle, and the relative magnitudes fluctuated substantially. The profile behaviors were quite complex and showed that the net radial flow direction varied from inward to outward during a cycle. As expected, the absolute magnitudes were considerably larger for the strongly forced condition. For regions immediately above the fuel tube, the radial velocities also varied with phase, but the flow was generally always toward the centerline with the velocity magnitude decreasing as the flow approached the centerline.

The flow behavior indicated by the near-field axial and radial velocity component measurements was qualitatively confirmed by phase-resolved shadowgraphs generated at the base of the flame and shown in Figs. 10 and 11 for the moderate and strong cases, respectively. A shadowgraph is sensitive to the second derivative of the index of refraction, which near the flame base is primarily indicative of the temperature gradient field. Cooler regions are emphasized more strongly in the shadowgraphs. The injection of cool fuel (brighter region) at the base of the flame can be clearly seen in the shadowgraphs during phases when the flow velocities were increasing (phases 70–0% for the moderate case and 60–90% for the strong case). In addition, the shadowgraphs showed clearly the clipping and lifting process the flames underwent during an excitation cycle. Heated gases were pushed towards the center as cool ambient air was drawn in. In both flame cases, clip-off occurred when the diameter of the heated gases above the burner was near a minimum. Strong mixing of cool and hot regions was clearly visible in the shadowgraphs, especially at the bases of the clipped flames. In support of an attached flame at the lip of the fuel tube, the shadowgraphs
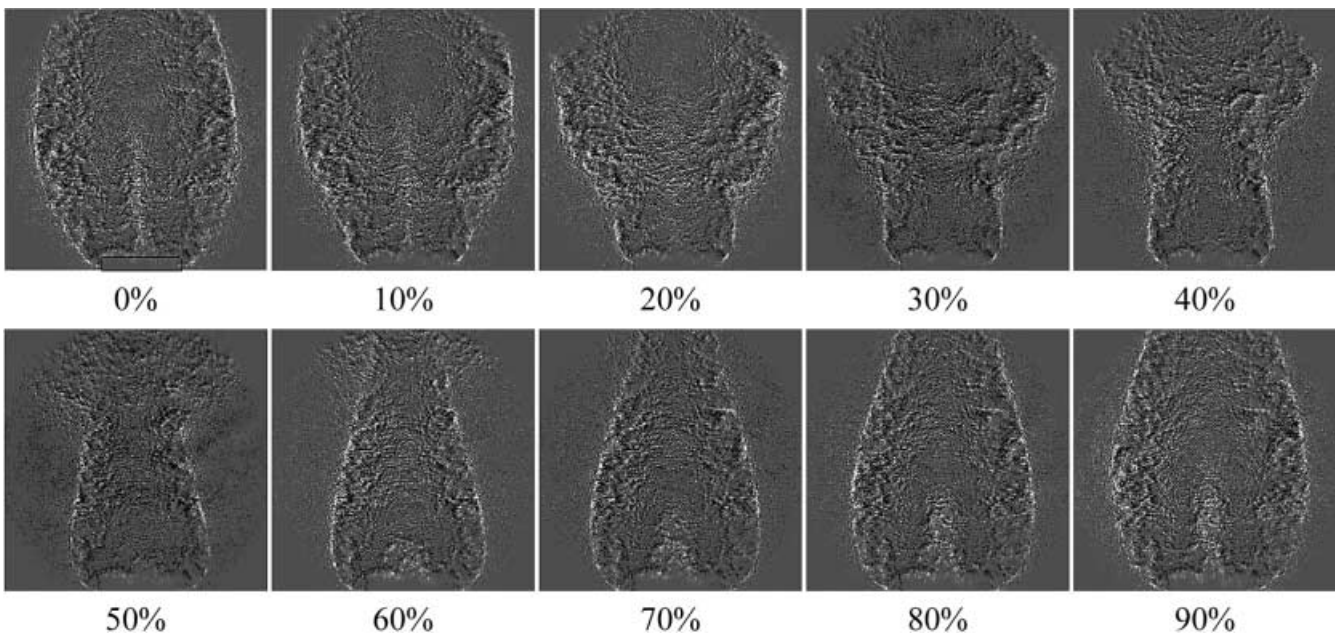

Fig. 10. Shadowgraphs of the moderately flickering flame case
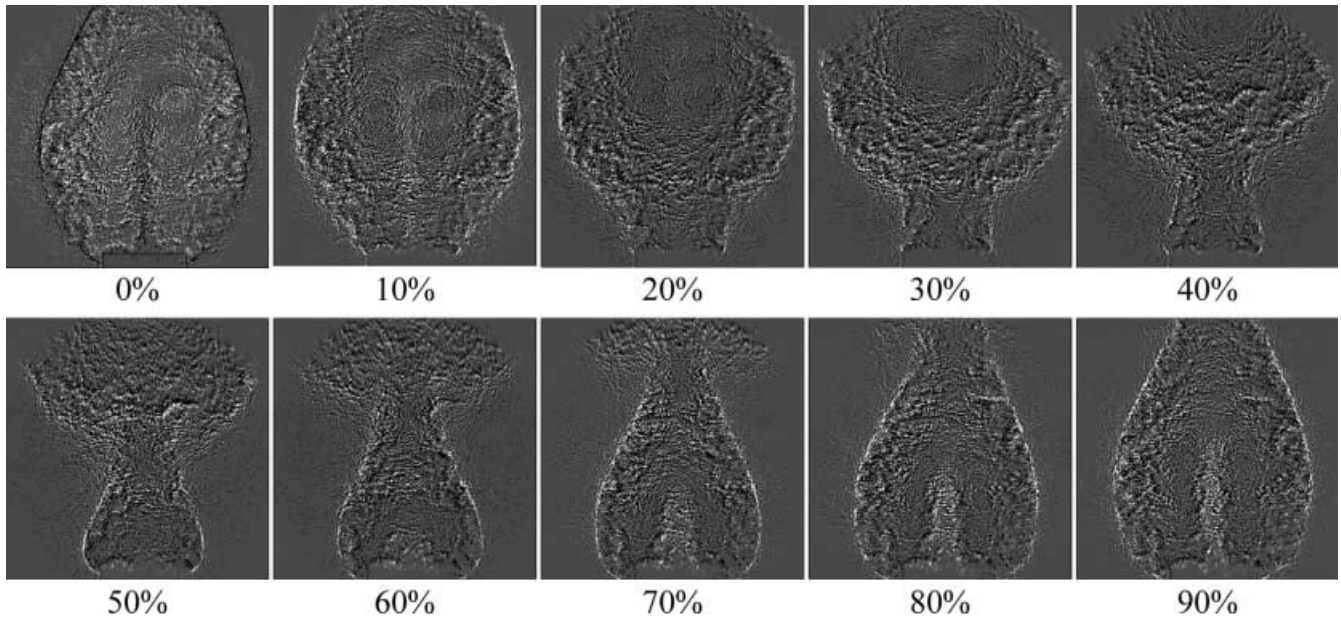
Fig. 11. Shadowgraphs of the strongly flickering flame case

showed a continuous region of ray coalescence extending below the tube exit in most of the phases, which is indicative of a heated region lying below the exit level.

Furthermore, the outside boundary of the shadowgraphs is marked by a bright, sharp region indicating ray coalescence that is due to temperature gradients. Such temperature gradients are strongly influenced by the mixing of cool co-flow air and hot gases arising from the existence of vortical structures. It is, then, no surprise that the curvature of this outer region of ray coalescence in the shadowgraph follows well the curvature of the regions of vorticity calculated from the velocity data (Fig. 6). Thus, the shadowgraphs further support, at least qualitatively, the important role vortical structures play in the clipping process of the present flame.

If the initial velocity profiles measured for each condition are averaged over one flame excitation cycle, then a steady-state equivalent velocity profile is obtained. The results of such averaging are shown in Fig. 12 for the first few millimeters above the exit of the fuel tube. The effect of forcing on the cycle-averaged initial velocity development is significant. Slight profile asymmetries aside, the W velocity profiles indicated that, for the moderately forced case, there existed a velocity deficit in the core of the fuel jet, which disappeared approximately 8 mm downstream of the tube exit as the shear layers merged. On the other hand, the strongly forced cycle-averaged profiles of W showed an accelerating fuel jet core, which drew on the momentum of the shear layers and thus contributed early to the development of strong vortical flow towards the center of the flame.

Integrating the cycle-averaged W profiles over the exit area of the fuel tube gave the bulk cycle-averaged velocity at each station, shown in Fig. 13. At the closest measurement point ($z=0.3$ mm) the integration gave bulk velocities of $W_b=0.079\pm0.005$ m/s and $W_b=0.077\pm0.007$ m/s for the moderately and strongly forced cases,

respectively. These values agreed quite well (less than 2% off) with the established flow rate through the fuel tube as controlled by the mass controller, thus giving
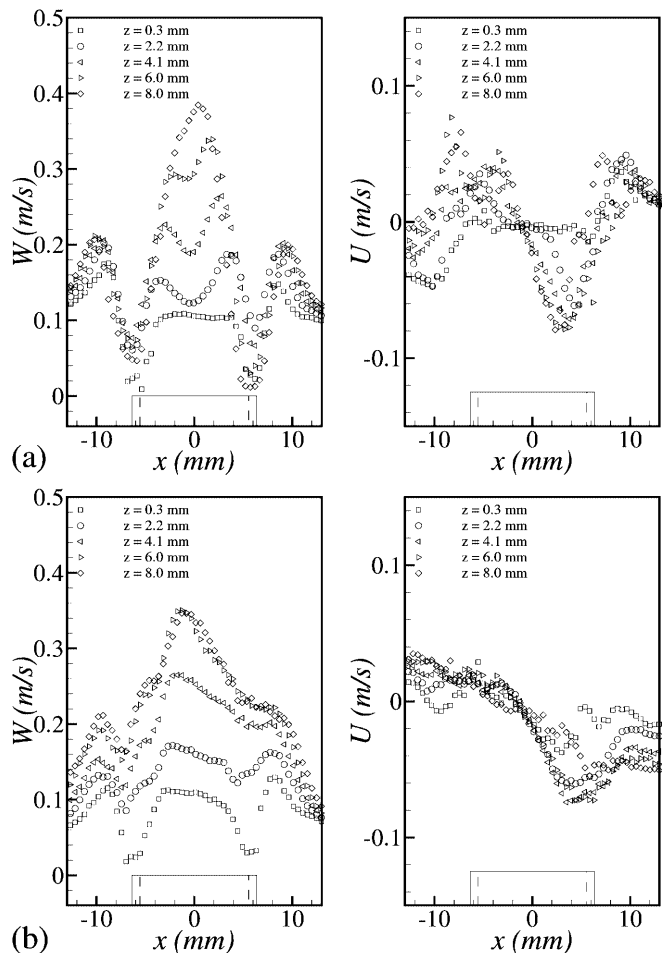

Fig. 12a, b. Velocity profiles averaged over one flame excitation cycle: **a** weakly forced case; **b** strongly forced case
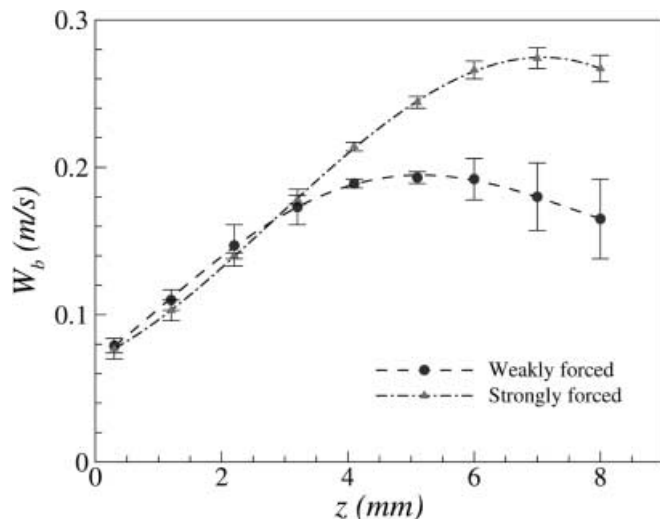
Fig. 13. Cycle-averaged bulk vertical velocity across the fuel jet exit at different elevations for the weakly and strongly forced flame cases. Measurements in the time-varying flames

confidence in the PIV measurements. Bulk velocities for the strongly forced case increased to higher values in comparison with the moderately forced case, indicating that stronger forcing resulted in greater co-flow entrainment early on.

4
Conclusions

Phase-locked measurements of the velocity field in the centerplane of an acoustically forced methane–air diffusion flame were performed using PIV. These measurements complement an existing database of other phase-locked information recorded for the two flame cases considered herein. The results demonstrated the importance of vortical structures on the dynamics and topology of these flames.

Velocity profiles recorded near the burner provided the first quantification of the effects of acoustic forcing on the initial fuel flow velocity. The induced fluctuations were quite large relative to the time-averaged initial flow velocity, even becoming negative for significant fractions of the flame cycle. However, it is important to keep in mind that the fluctuations were relatively minor when compared with the ultimate velocities attained in these buoyancy-dominated flames. Earlier modeling results for the moderate forcing case (Kaplan et al. 1996) were found to be highly sensitive to the initial velocity radial profile shape (personal communication, Smyth, December 2000). It is hoped that the improved characterization of the initial flow conditions provided by this work will lead to more realistic modeling of these flames and ultimately

result in a better understanding of flow field/combustion coupling.

References

Cetegen BM, Ahmed TA (1993) Experiments on the periodic instability of buoyant plumes and pool fires. Combust Flame 93:157–184

Cetegen BM, Dong Y (2000) Experiments on the instability modes of buoyant diffusion flames and effects of ambient atmosphere on the instabilities. Exp Fluids 28:546–558.

Everest DA, Shaddix CR, Smyth KC (1996) Quantitative two-photon laser-induced fluorescence imaging of CO in flickering CH4/air diffusion flames. Proc Combust Inst 26:1161–1169

Hamins A, Yang JC, Kashiwagi T (1992) An experimental investigation of the pulsation frequency of flames. Proc Combust Inst 24:1695–1702

Kaplan CR, Shaddix CR, Smyth KC (1996) Computations of enhanced soot production in time-varying CH4/air diffusion flames. Combust Flame 106:392–405

Lewis GS, Cantwell BJ, Vandsburger U, Bowman CT (1988) An investigation of the structure of a laminar non-premixed flame in an unsteady vortical flow. Proc Combust Inst 22:515–521

Lingens A, Reeker M, Schreiber M, (1996) Instability of buoyant diffusion flames. Exp Fluids 20:241–248

Madsen AH, McCluskey DR (1994) On the accuracy and reliability of PIV measurements. Paper presenetd at the Seventh International Symposium on the Application of Laser Techniques to Fluid Mechanics, 11–14 July, Lisbon, Portugal

Pitts WM (1996) Thin-filament pyrometry in flickering laminar diffusion flames. Proc Combust Inst 26:1171–1179

Pitts WM, Smyth KC, Everest DA (1998) Effects of finite time response and soot deposition on this filament pyrometry measurements in time-varying diffusion flames. Proc Combust Inst 27:563–569

Renard P-H, Thévenin D, Rolon JC, Candel S (2000) Dynamics of flame/vortex interactions. Prog Energy Combust Sci 26:225–282

Santoro RJ, Semerjian HG, Dobbins RA (1983) Soot particle measurements in diffusion flames. Combust Flame 51:203–218

Shaddix CR, Smyth KC (1996) Laser-induced incandescence measurements of soot production in steady and flickering methane, propane, and ethylene diffusion flames. Combust Flame 107:418–452

Shaddix CR, Harrington JE, Smyth KC, (1994) Quantitative measurements of enhanced soot production in a flickering methane/air diffusion flame. Combust Flame 99:723–732

Skaggs RR, Miller JH (1996) Tunable diode laser absorption measurements of carbon monoxide and temperature in a time-varying, methane/air, non-premixed flame. Proc Combust Inst 26:1181–1188

Smyth KC (2000) Diffusion flame measurements of species concentrations, soot concentrations, temperature, and velocity. http://www.bfrl.nist.gov/865/flamedata/

Smyth KC, Harrington JE, Johnsson EL, Pitts WM (1993) Greatly enhanced soot scattering in flickering CH4/air diffusion flames. Combust Flame 95:229–239

Smyth KC, Shaddix CR, Everest DA (1997) Aspects of soot dynamics as revealed by measurements of broadband fluorescence and flame luminosity in flickering diffusion flames. Combust Flame 111:185–207

Strawa AW, Cantwell BJ (1985) Visualization of the structure of a pulsed methane–air diffusion flame. Phys Fluids 28:2317–2320

Zhang J, Megaridis CM (1998) Soot microstructure in steady and flickering laminar methane/air diffusion flames. Combust Flame 112:473–484